Analog transitions in sd- and f-shell nuclei and the isovector part of optical potentials studied by the (p,n) reaction at 35 MeV

G. C. Jon,[1] H. Orihara,[2] T. Niizeki,[3] M. Oura,[2] K. Ishii,[2] A. Terakawa,[2] M. Hosaka,[2] K. Itoh,[2] C. C. Yun,[2] Y. Fujii,[4]
T. Nakagawa,[4] K. Miura,[5] and H. Ohnuma[6]

[1]*Institute of Physics, Academia Sinica, Nankang Taipei, Taiwan 11592*
[2]*Cyclotron and Radioisotope Center, Tohoku University, Sendai 980-77, Japan*
[3]*Department of Physics, Tokyo Institute of Technology, Tokyo 152, Japan*
[4]*Department of Physics, Tohoku University, Sendai 980-77, Japan*
[5]*Tohoku Institute of Technology, Sendai 982, Japan*
[6]*Department of Physics, Chiba Institute of Technology, Chiba 275, Japan*

Quasielastic (p,n) reactions on sd- and f-shell nuclei were studied at an incident proton energy of 35 MeV. Differential cross sections for isobaric analog $\Delta J^{\pi}=0^+$ (Fermi-type) transitions and their angular distributions were measured in 13 $N>Z$ target nuclei ranging $17 \leq A \leq 48$, ^{17,18}O, ^{22}Ne, ^{25,26}Mg, ^{27}Al, ^{30}Si, ^{34}S, ^{38,40}Ar, and ^{42,44,48}Ca. Pure $\Delta J^{\pi}=0^+$ Fermi-type transitions were observed in six of them. As for the other seven nuclei, contributions from mixed $\Delta J^{\pi} \neq 0^+$ components or those from unresolved transitions were evaluated by microscopic distorted-wave Born approximation (DWBA) calculations to subtract them from the raw data and extract pure Fermi-type transition strengths. Thus a total of 13 $\Delta J^{\pi}=0^+$ angular distributions was fitted by macroscopic DWBA calculations with a Lane-model optical potential to derive systematically the isovector part of the potential. The best-fit parameters for each target are presented. A-dependent global parameters were obtained from these best-fit parameters by a least-squares fit. [S0556-2813(97)04408-7]

PACS number(s): 25.40.Ep, 27.20.+n, 27.30.+t, 27.40.+z

I. INTRODUCTION

Analog transitions have been studied for $N>Z$ nuclei with isospin $T_0=(N-Z)/2$, for which the (p,n) reaction excites final states with $T=T_0$ as well as those with $T=T_0 \pm 1$. The $T=T_0$ states, having a similar nature to the parent state, are referred to as isobaric analog states (IAS's). The (p,n) transition to the ground-state analog is regarded as elastic scattering with the isospin z component flipped and is hence sometimes called quasielastic scattering. It corresponds to Fermi-type β decay. Quasi-inelastic scattering, those to excited state analog states (EAS's) such as 2^+, 3^-, and 4^+, have also been observed.

The Lane-model optical potential is often used in macroscopic distorted-wave Born approximation (DWBA) analyses of the quasiscattering. It is expressed as [1]

$$U(r) = -U_0(r) + (4/A)U_1(r)\vec{t}\cdot\vec{T} + U_{so}(r) + (1/2-t_z)V_c(r),$$ (1)

where $\vec{t}(\vec{T})$ is the projectile (target) isospin, U_{so} is the spin-orbit potential, and V_C is the Coulomb potential. The isospin dependent $(\vec{t}\cdot\vec{T})$ term yields t_+T_-, t_-T_+, and t_ZT_z, corresponding to (p,n), (n,p), and (p,p) or (n,n) reactions, respectively. Then the (p,n) quasiscattering takes place through the term

$$U_{pn}(r) = (2/A)\sqrt{N-Z}\,U_1(r).$$ (2)

The isovector potential U_1 is usually parametrized in terms of standard Woods-Saxon forms as

$$U_1(r) = V_1 f(x_R) - 4ia_I W_1 \frac{d}{dx_I}f(x_I),$$

$$f(x) = (1+e^x)^{-1}, \quad x=(r-R_i)/a_i,$$

$$R_i = r_i A^{1/3} \quad (i=R \text{ or } I).$$ (3)

In a macroscopic treatment, V_1 and W_1 in Eq. (3) are dependent on energy and mass, and are directly determined by the strength of the ground-state analog transition. In a microscopic treatment, on the other hand, the analog transition takes place through the isospin-dependent part $(\tau\tau)V_\tau f(r)$ of the effective interaction, which is derived from G-matrix elements based on the free nucleon-nucleon interaction.

Knowledge of U_{pn} gives measures of the strengths of the quasi-inelastic scattering leading to excited analog states [2–4] as well. Recently, particular attention has been paid to the isovector potential strength. It plays a dominant role for coupling between the giant isovector monopole state and the isobaric analog state, yielding a spreading width for the latter [5]. Studies of Fermi-type transitions to the IAS by the (p,n) reaction present a good place to explore this potential. Carlson and his collaborators reported [6] a systematic optical model analysis of quasielastic (p,n) reactions at 22.8 MeV on 29 nuclei ranging from ^{9}Be to ^{208}Pb. They derived U_1 for each target nucleus and gave a smooth parametrization of the best-fit parameters in U_1 for all the nuclei investigated. However, their data and analysis were limited by experimental conditions and the theoretical treatment of mixed analog transitions.

(p,n) reactions available for a study of *pure* Fermi-type transitions in sd- and f-shell nuclei have been limited to a
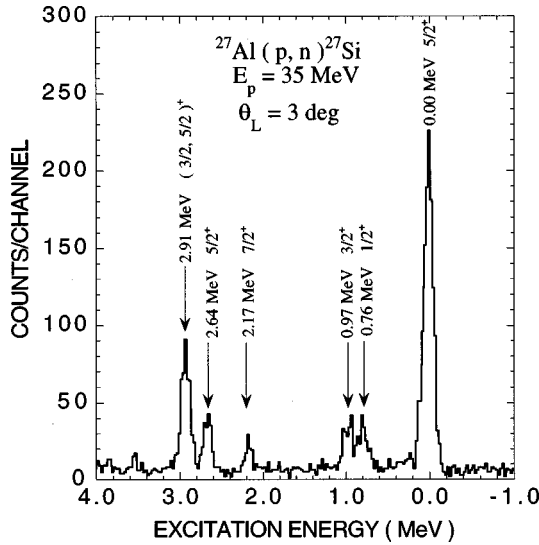
FIG. 1. Sample excitation energy spectrum of neutrons leading to the low-lying states in ^{27}Si following the ^{27}Al$(p,n)^{27}$Si reaction taken at 3° with a flight path of 44.3 m. Energy per bin is 25 keV.

FIG. 3. Differential cross sections for neutrons leading to the unresolved 0.937(3$^+$), 1.042(0$^+$, IAS), 1.081(0$^+$), and 1.121(5$^+$) MeV states in ^{18}F. The notation is the same as in Fig. 2.

few cases so far. In a medium and heavy nucleus, the IAS is located in a high enough excitation energy region where contributions from nearby states may be regarded as continuum backgrounds. However, significant contaminations to the Fermi transition come from closely located discrete levels in light nuclei. A typical example is ^{18}F, whose IAS is located within 184 keV of the 3$^+$, 5$^+$, and 0$^-$ states. For an odd-mass target nucleus, several ΔJ^π components can be mixed in the transition to the IAS, even if it is an isolated state. Investigation of the (p,n) reaction at 35 MeV with high-
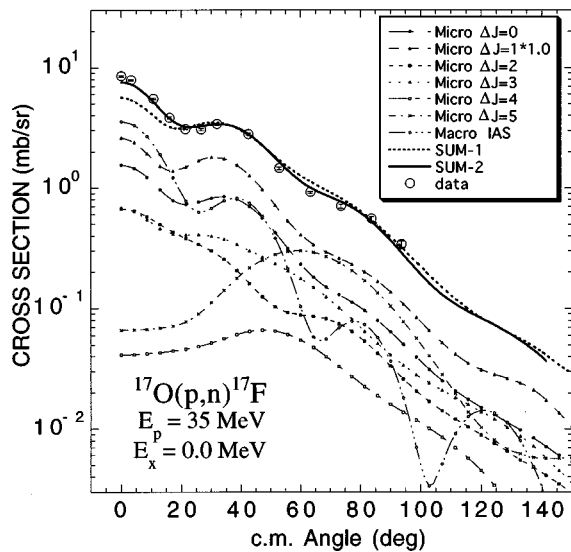

FIG. 2. Differential cross sections for neutrons leading to the ground state of ^{17}F. The curves are DW results for the 5/2$^+ \rightarrow$ 5/2$^+$ transition for each ΔJ^π. The line denoted by "Macro IAS" is the macroscopic calculation using the isovector potential with the best-fit parameters obtained in the present study. The line denoted by "SUM-1" shows the sum over microscopic predictions for all ΔJ^π including a $\Delta J^\pi = 0^+$ Fermi-type transition, while that denoted by "SUM-2" shows the same except that the $\Delta J^\pi = 0^+$ calculation is replaced by "Macro IAS."
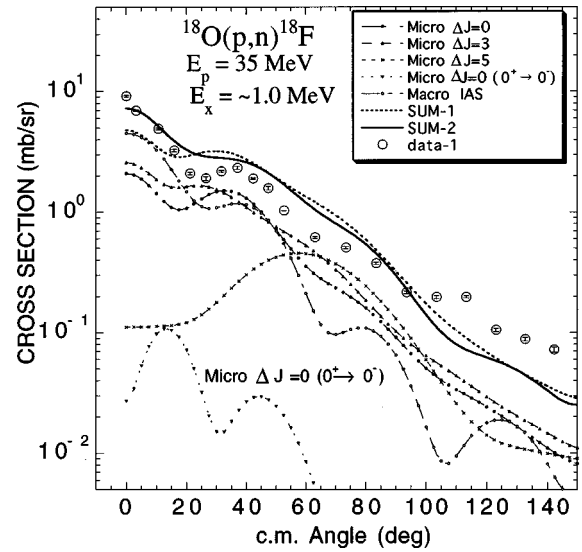
resolution experiments [7–10], together with well-established effective nucleon-nucleon interactions and recently advanced shell-model one-body-transition-densities (OBTD's), allows us to evaluate $\Delta J^\pi \neq 0^+$ components theoretically and makes it possible to find the $\Delta J^\pi = 0^+$ Fermi-type component separately for a number of (p,n) reactions on sd-shell nuclei. In Ref. [10] we have explained successfully the differential cross sections for the composite peak corresponding to the IAS, and the 3$^+$, 5$^+$, and 0$^-$ states in ^{18}F by a sum of macroscopic DWBA predictions for the $0^+ \rightarrow 0^+$ Fermi-type transition and microscopic DWBA predictions for the other transitions. Similarly the 5/2$^+ \rightarrow$ 5/2$^+$ transition in the ^{17}O$(p,n)^{17}$F(g.s.) reaction could be decomposed to $\Delta J^\pi = 0^+ - 5^+$ components in Ref. [10]. It was also found that microscopic DWBA analyses successfully reproduce absolute values of the (p,n) cross sections between 20° and 90° for most $\Delta J^\pi = 2^+$, 3$^+$, and 5$^+$ transitions observed in ^{22}Ne, ^{24}Mg, and ^{34}S [7–9]. Systematic microscopic analyses of the data were reported in these papers using Brown-Wildenthal (BW) wave functions [11], for which a stringent test with the charge-exchange reaction has been carried.

In this paper we extend our previous work of Refs. [7–10] and discuss the isovector part of the Lane potential based on experimental data of (p,n) reactions at $E_p = 35$ MeV on a variety of target nuclei ranging $17 \leq A \leq 48$, namely, ^{17,18}O, ^{22}Ne, ^{25,26}Mg, ^{27}Al, ^{30}Si, ^{34}S, ^{38,40}Ar, and ^{42,44,48}Ca.

II. EXPERIMENTAL PROCEDURE

The experiment was performed at the Cyclotron and Radioisotope Center, Tohoku University, with a 35-MeV proton beam from an AVF-cyclotron and a beam swinger system. The details of the experimental setup have been described previously [12,13]. Neutron energies were measured by the time-of-flight (TOF) technique, where neutrons were detected by a detector array located at 44.3 m from the target. The detectors, 23.2 l in a total sensitive volume, were filled with organic liquid scintillator NE213. The absolute
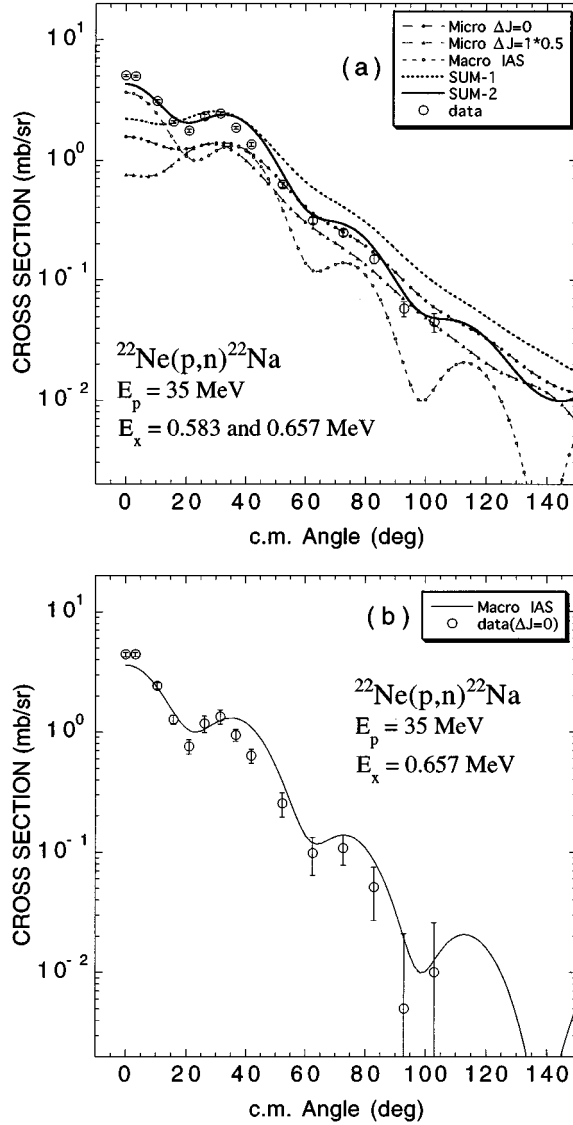
FIG. 4. (a) Differential cross sections for neutrons leading to the unresolved 0.583(1$^+$) and 0.657(0$^+$, IAS) MeV states in ^{22}Na. The notation is the same as in Fig. 2, except that the microscopic calculation for $\Delta J^\pi = 1^+$ is multiplied by 0.5. (b) Differential cross sections for neutrons leading to the 0.657-MeV IAS in ^{22}Na. The points with error bars (denoted as "Data") are obtained by subtracting the contribution of the 0.583-MeV 1$^+$ state shown by the dashed line in (a) as described in the text. The dotted line is the result of macroscopic DW calculation with the best-fit parameters for the isovector potential.

FIG. 5. (a) Same as Fig. 2, but for the ^{25}Mg$(p,n)^{25}$Al reaction. The calculated $\Delta J^\pi = 1^+$ cross sections are multiplied by 0.6. (b) Differential cross sections for the $\Delta J^\pi = 0^+$ transition leading to the ground state of ^{25}Al. "Data" are obtained by subtracting the $\Delta J^\pi = 1^+$, 2$^+$, 3$^+$, 4$^+$, and 5$^+$ contributions from the raw data. The dotted line shows the macroscopic DW calculation obtained with the best-fit parameters for the isovector potential.

efficiencies of the detectors were obtained from the ^{7}Li$(p,n)^7$Be activation analyses with an error less than $\pm 6\%$. Errors in the absolute magnitude of (p,n) cross sections were estimated to be less than 12%. All the targets were enriched isotopes with enrichments better than 95%. Two kinds of gas cell were used for the ^{17,18}O, ^{22}Ne, and ^{38}Ar targets; one of them was of a disk shape 2 cm long and 1 cm in diameter with thin windows, and the other was of a cylindrical shape 20 cm long and 2 cm in diameter. The former, filled with 400 torr gas, was used for measurements at small angles ($\leqslant 35°$), while the latter was used at large angles. In the latter case, neutron detectors did not see the windows. More details about the gas target, choice of window material,
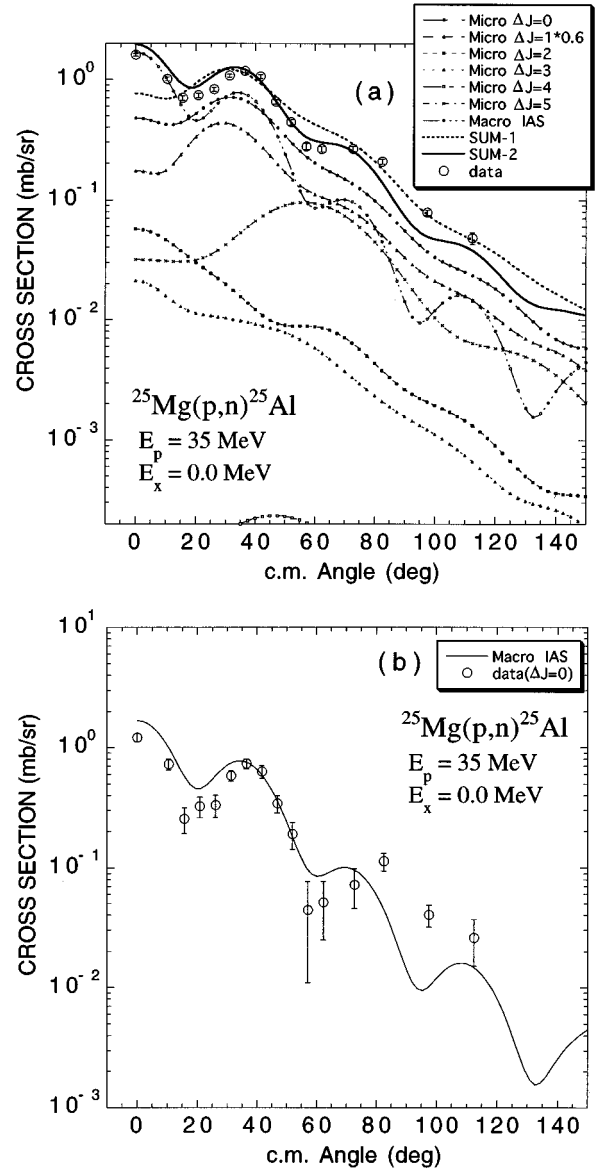
and background subtraction method in particular are described in Ref. [10]. Metallic foil was used for ^{25,26}Mg and ^{42,44,48}Ca. The Ca targets were fabricated by vacuum evaporation. The ^{30}Si target was ^{30}SiO foil, while the ^{34}S target was prepared by evaporating the element onto enriched ^{12}C foil.

The overall neutron energy resolution was typically 160 keV. Figure 1 illustrates a typical excitation energy spectrum of neutrons leading to the low-lying states in ^{27}Si following the ^{27}Al$(p,n)^{27}$Si reaction. In Figs. 2–14, the angular distributions of the cross section are presented. The lines in the figures are microscopic and macroscopic DWBA predictions described below.
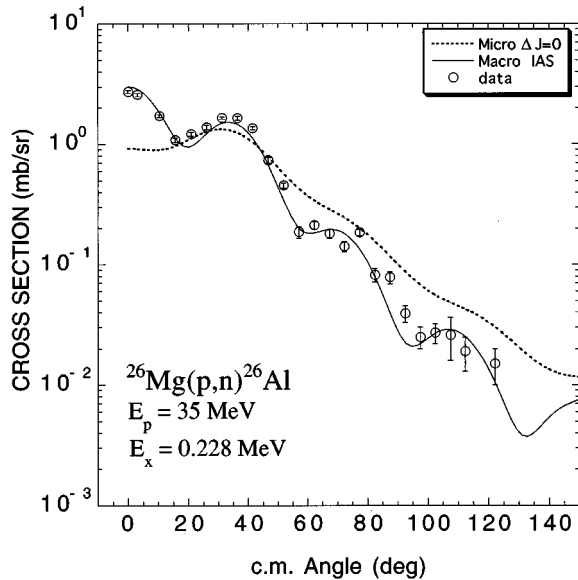
FIG. 6. Differential cross sections for neutrons leading to the 0.228-MeV IAS in ^{26}Al. This is an example of pure IAS transitions. The solid line shows the macroscopic DW calculation obtained with the best-fit parameters for the isovector potential, and the dotted line shows microscopic DW calculation.

III. MICROSCOPIC DWBA APPROXIMATION FOR THE (*p*,*n*) REACTION

Out of 13 target nuclei studied in the present work, pure IAS transitions were observed in six nuclei. For the other seven nuclei, it was necessary to subtract contributions from unresolved peaks or those from $\Delta J^{\pi} \neq 0^{+}$ components. In this section, we describe the procedure of microscopic DWBA calculations needed to extract cross sections for the pure $\Delta J^{\pi} = 0^{+}$ Fermi-type transition from the raw data by subtracting other contributions.

The data were first compared with microscopic DW results calculated by the computer code DWBA-74 [14], which includes knock-on exchange effects in an exact manner. Note that fully antisymmetrized calculations were made in the present microscopic DW analysis, in which non-normal parity terms such as $\Delta J(\Delta L, \Delta S) = 1(1,0)$ for the $0^{+} \rightarrow 1^{+}$ transition also contribute to the cross section. The optical potential parameters of Becchetti and Greenlees [15] were used for the entrance channel. Those for the exit channel were self-consistent potential parameters derived by Carlson *et al.* [6]. The effective nucleon-nucleon interactions used in the present DW analysis were those by Bertsch *et al.* (M3Y) [16]. The sensitivity of such calculations to the optical-potential parameters is elaborated in Ref. [17].

Spectroscopic amplitudes (OBTD's) for the microscopic DWBA analysis were obtained from full *sd*-shell model calculations [18] using the code OXBASH with the *A*-dependent interaction of Wildenthal [11]. As for *f*-shell nuclei, the full *fp* potential by Richter [19] has been used to calculate OBTD's in this region. Single-particle radial wave functions used in DW calculations were generated in a Woods-Saxon potential with $r_0 = 1.25$ fm, $a = 0.6$ fm, and $V_{LS} = 6$ MeV and the depth adjusted to reproduce the binding energy of a valence nucleon.

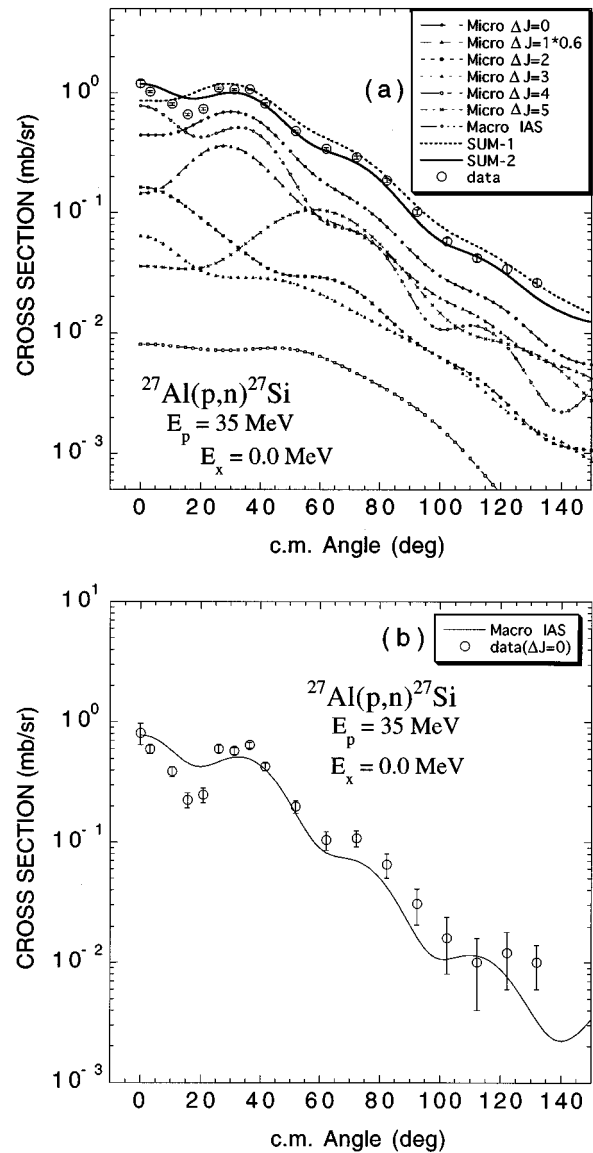In Figs. 6, 9, and 11–14 experimental cross sections are

FIG. 7. (a) Same as Fig. 2, but for the ^{27}Al(p,n)^{27}Si reaction. Calculated $\Delta J^{\pi} = 1^{+}$ cross sections are multiplied by 0.5. (b) Differential cross sections for the $\Delta J^{\pi} = 0^{+}$ transition leading to the ground state of ^{27}Si. ''Data'' are obtained by subtracting the $\Delta J^{\pi} \neq 0^{+}$ contributions from the raw data. The dotted line shows the macroscopic DW calculation obtained with the best-fit parameters for the isovector potential.

compared with DWBA predictions for the (*p*,*n*) reactions on ^{26}Mg, ^{34}S, ^{40}Ar, ^{42}Ca, ^{44}Ca, and ^{48}Ca, in which the IAS is either an isolated level or no significant closely lying transitions are predicted by the shell-model calculation, or smooth continuum backgrounds can be easily subtracted. For example, the contribution of the 0.15-MeV 3^{+} state in the IAS ground-state peak in ^{34}Cl is negligibly small as shown in Fig. 1 of Ref. [7]. The dashed lines are microscopic DWBA predictions for the IAS. The experimental cross sections around the first maximum at $\sim 30°$ are well explained by the microscopic calculation, although overall shapes of angular distributions are better reproduced by macroscopic calculations which are shown by the solid lines and will be described later. Such a failure of microscopic calculations for
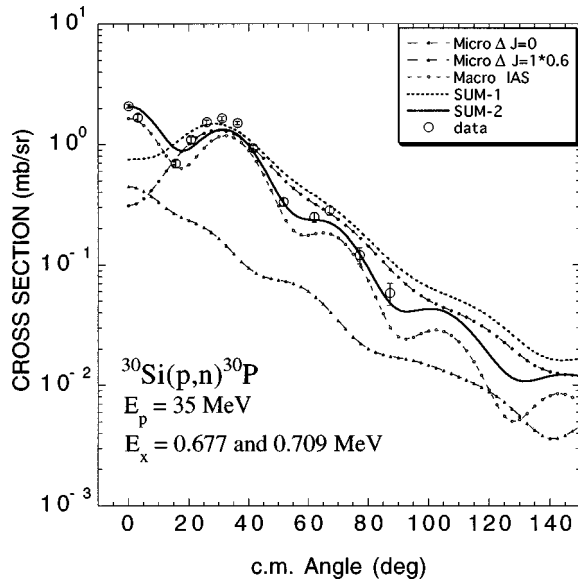
FIG. 8. Differential cross sections for neutrons leading to the $0.677(0^+$, IAS) and $0.709(1^+)$ MeV states in ^{30}P. See also caption to Fig. 4(a).

IAS transitions was noted before [7–10] and ascribed to the "collectivity" of the IAS transition, namely, due to numerous small components not included in shell-model calculations adding up coherently in the IAS transition especially at large angles. Nevertheless, the IAS cross sections near the first maximum, where only major components contribute, have been found well reproduced by microscopic calculations [7–10]. Differences between the experimental cross sections and microscopic DWBA cross sections around 30° are less than ±12% for *sd*-shell nuclei.

The IAS transition in the ^{18}O$(p,n)^{18}$F reaction is shown in Fig. 3. In this case the measured IAS cross sections include those to the 0^-, 3^+, and 5^+ states, which were not resolved experimentally. Analysis of this reaction is detailed in our previous paper [10]. Cross sections for the 3^+ ground
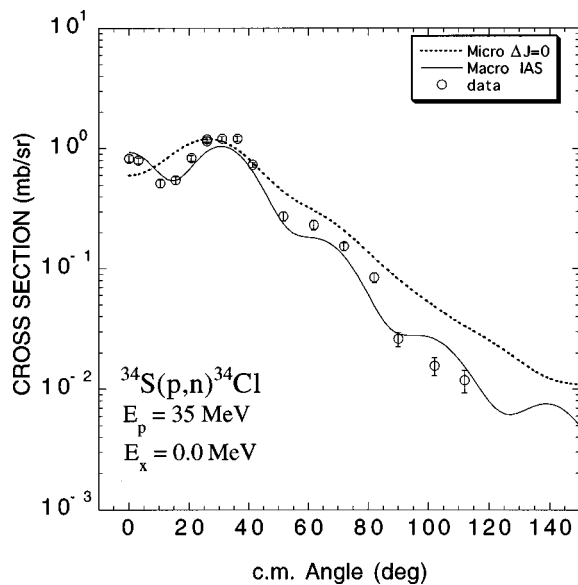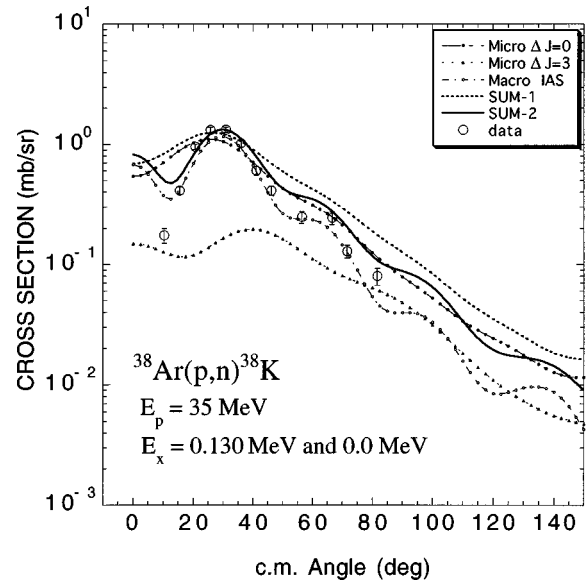

FIG. 10. Differential cross sections for neutrons leading to the 0.13-MeV IAS and ground state (3^+) in ^{38}K. The dashed line with solid triangles show calculated $\Delta J^\pi=3^+$ cross sections for the ground state. The notation is the same as in Fig. 2.

state, which was not resolved from the 0.130-MeV IAS in ^{38}K, is small but not negligible as shown in Fig. 10.

The angular distributions for the (p,n) reaction on ^{22}Ne and ^{30}Si are shown in Figs. 4 and 8. In these cases a 1^+ state which has sizable (p,n) strength exists near the IAS. As is well known, the Gamow-Teller-type $0^+ \rightarrow 1^+$ (p,n) transition is quenched. Therefore measured cross sections around the 30° maximum were fitted by the sum of calculated $0^+ \rightarrow 0^+$ and $0^+ \rightarrow 1^+$ cross sections by adjusting a normalization factor for the latter. A normalization factor of 0.5 and 0.6 was found to fit the data for ^{22}Ne and ^{30}Si, respectively.

The angular distributions shown in Figs. 2, 5, and 7 are those for (p,n) reactions on odd-mass nuclei ^{17}O, ^{25}Mg, and ^{27}Al. Six components with $\Delta J^\pi=0^+$, 1^+, 2^+, 3^+,

FIG. 9. Differential cross sections for neutrons leading to the ground state (0^+, IAS) of ^{34}Cl. See also caption to Fig. 6.
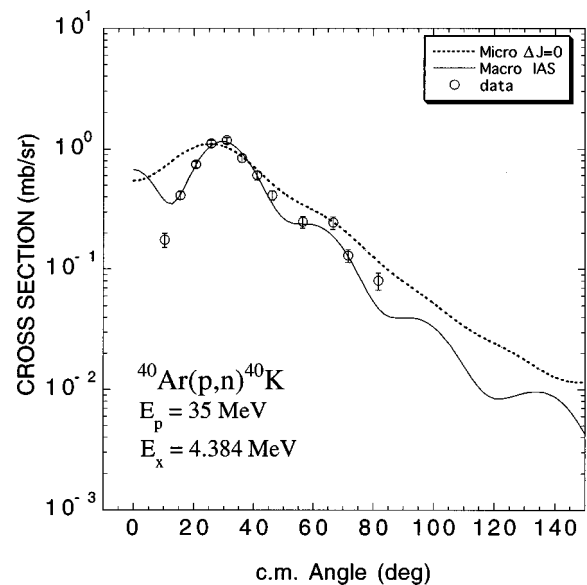

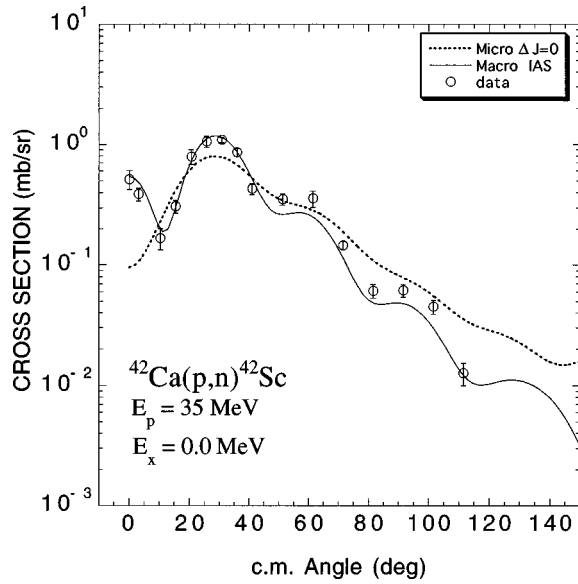FIG. 11. Differential cross sections for neutrons leading to the 4.384-MeV IAS in ^{40}K. See also caption to Fig. 6.

FIG. 12. Differential cross sections for neutrons leading to the ground state (0^+, IAS) of ^{42}Sc. See also caption to Fig. 6.

FIG. 14. Differential cross sections for neutrons leading to the 6.677-MeV IAS in ^{48}Sc. See also caption to Fig. 6.

4^+, and 5^+ contribute to the cross sections for these $5/2^+ \rightarrow 5/2^+$ transitions. Fitting the data around 30° by an incoherent sum of DWBA cross sections for each ΔJ^π with only a normalization factor for the $\Delta J^\pi = 1^+$ transition as an adjustable parameter, we find a normalization factor of 1.0 for ^{17}O, as reported in Ref. [6], and 0.6 for ^{25}Mg and ^{27}Al.

For ^{17,18}O, ^{22}Ne, ^{25}Mg, ^{27}Al, ^{30}Si, and ^{38}Ar(p,n), the cross sections for the pure $\Delta J^\pi = 0^+$ transitions were obtained by subtracting the microscopic contributions other than $\Delta J^\pi = 0^+$ from the data. Typical examples thus obtained for ^{22}Ne$(p,n)^{22}$Na* ($E_{exc} = 0.657$ MeV, IAS) and ^{25}Mg$(p,n)^{25}$Al (g.s., $\Delta J^\pi = 0^+$ component) are illustrated in Figs. 4(b) and 5(b), respectively. The curves are macroscopic DWBA calculations predicted with best-fit isovector potential parameters described below. Good fits observed here jus-
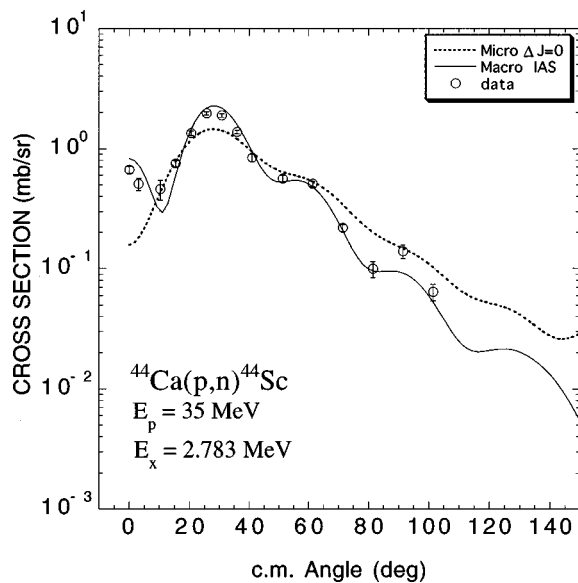
tify the above-mentioned method for subtraction of other components. These angular distributions therefore were used as ''experimental data for pure Fermi-type transitions'' for the parameter search described in the following section, together with six transitions in ^{26}Mg, ^{34}S, ^{40}Ar, and ^{42,44,48}Ca.

IV. MACROSCOPIC DWBA ANALYSIS AND PARAMETER SEARCH FOR ISOVECTOR POTENTIAL

Assuming that the (p,n) reaction leading to the IAS is caused by the isovector potential expressed as Eq. (3), which has a volume-type real part and a surface-type imaginary part, the parameters to be determined are the potential depths

FIG. 15. Best-fit values of V_1 and W_1 plotted as a function of $A^{1/3}$. The solid lines indicate results of least-squares fit with errors shown by the dotted ($+\sigma$) and dot-dashed ($-\sigma$) lines calculated from error matrices.

FIG. 13. Differential cross sections for neutrons leading to the 2.783-MeV IAS in ^{44}Sc. See also caption to Fig. 6.

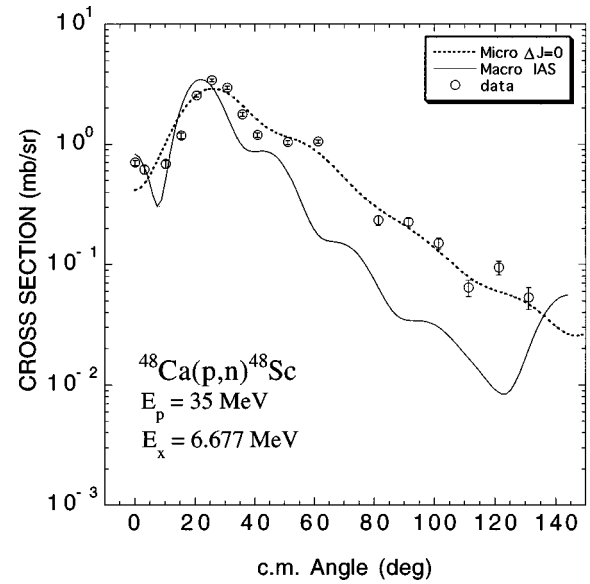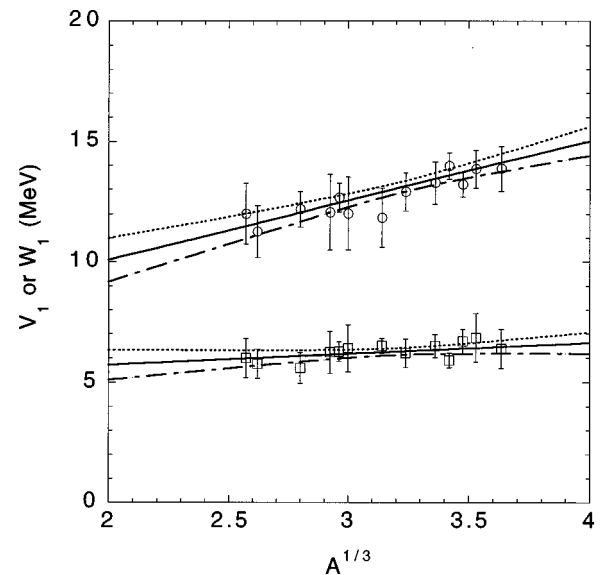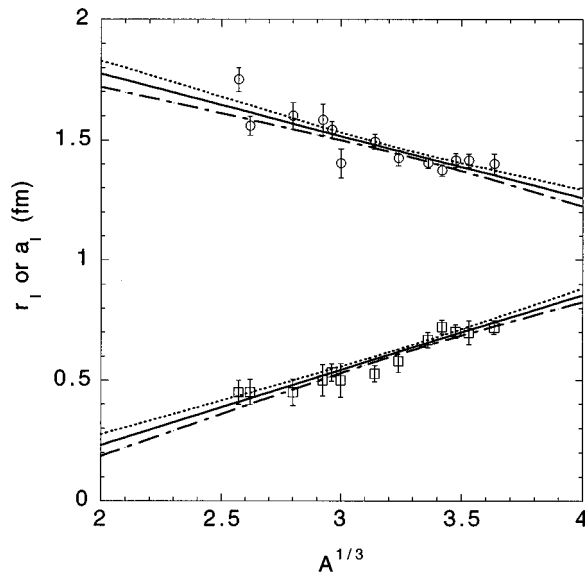TABLE I. Best-fit parameters of isovector potential or each nucleus.

Reaction	E_{exc} of IAS (MeV)	V_1 (MeV)	W_1 (MeV)	r_I (fm)	a_I (fm)
$^{17}O(p,n)^{17}F$	0.0	12.00 ± 1.25	6.00 ± 0.80	1.750 ± 0.050	0.450 ± 0.050
$^{18}O(p,n)^{18}F$	1.041	11.26 ± 1.08	5.76 ± 0.60	1.560 ± 0.039	0.451 ± 0.053
$^{22}Ne(p,n)^{22}Na$	0.657	12.19 ± 0.73	5.59 ± 0.63	1.600 ± 0.054	0.450 ± 0.055
$^{25}Mg(p,n)^{25}Al$	0.0	12.06 ± 1.56	6.24 ± 0.87	1.584 ± 0.065	0.500 ± 0.065
$^{26}Mg(p,n)^{26}Al$	0.228	12.66 ± 0.58	6.27 ± 0.40	1.543 ± 0.034	0.533 ± 0.036
$^{27}Al(p,n)^{27}Si$	0.0	11.00 ± 1.50	5.89 ± 0.98	1.403 ± 0.061	0.500 ± 0.070
$^{30}Si(p,n)^{30}P$	0.677	11.84 ± 1.22	6.50 ± 0.32	1.493 ± 0.032	0.528 ± 0.034
$^{34}S(p,n)^{34}Cl$	0.0	12.90 ± 0.78	6.20 ± 0.59	1.425 ± 0.033	0.580 ± 0.047
$^{38}Ar(p,n)^{38}K$	0.130	13.27 ± 0.87	6.50 ± 0.48	1.404 ± 0.023	0.668 ± 0.032
$^{40}Ar(p,n)^{40}K$	4.384	13.97 ± 0.55	5.90 ± 0.30	1.373 ± 0.024	0.722 ± 0.029
$^{42}Ca(p,n)^{42}Sc$	0.0	13.20 ± 0.50	6.69 ± 0.50	1.414 ± 0.029	0.704 ± 0.029
$^{44}Ca(p,n)^{44}Sc$	2.783	15.55 ± 0.97	7.69 ± 1.02	1.414 ± 0.050	0.699 ± 0.050
$^{48}Ca(p,n)^{48}Sc$	6.677	13.86 ± 0.93	6.38 ± 0.80	1.400 ± 0.029	0.720 ± 0.028

V_1 and W_1, geometrical parameters for the real part r_R and a_R, and those for the imaginary part r_I and a_I. To reduce the number of parameters to be fitted, the real geometrical parameters r_R and a_R were fixed to those by Becchetti and Greenlees [15], since these are usually taken as fixed in both entrance and exit channels when they are used in distorting potentials. Then we carried out a parameter search with the program IASEARCH [20] to find the best-fit parameter set to reproduce differential cross sections for each IAS transition. Finally, we found global relation for each parameter as a linear function of $A^{1/3}$ by a least-squares fit.

Table I lists the best-fit parameters obtained for each reaction. The radius of the imaginary potential decreases gradually, while the diffuseness parameter increases, as $A^{1/3}$ increases. The real potential depth V_1 increases as well. The imaginary potential depth W_1 seems to be almost constant in the mass region studied. These best-fit parameters are plotted as a function of $A^{1/3}$ in Figs. 15 and 16. It should be noted that the values obtained from the ''subtracted data'' lie

on a smooth line, confirming again the validity of the procedure described before and reliability of microscopic calculations. The solid lines indicate results of a least-squares fit assuming that all parameters are a linear function of $A^{1/3}$. Taking the diagonal and off-diagonal elements of the error matrices, we were able to describe the $A^{1/3}$ dependence of the potential parameters as

$$V_1 = 5.161 + 2.461 A^{1/3}$$
$$\pm \sqrt{5.521 - 2 \times 1.701 A^{1/3} + 0.5288 (A^{1/3})^2},$$

$$W_1 = 4.805 + 0.4529 A^{1/3}$$
$$\pm \sqrt{2.632 - 2 \times 0.8226 A^{1/3} + 0.2590 (A^{1/3})^2}, \quad (4)$$

and

$$r_1 = 2.289 - 0.2580 A^{1/3}$$
$$\pm \sqrt{0.01939 - 2 \times 0.005923 A^{1/3} + 0.001824 (A^{1/3})^2},$$

$$a_1 = -0.3940 + 0.3122 A^{1/3}$$
$$\pm \sqrt{0.01277 - 2 \times 0.003887 A^{1/3} + 0.001193 (A^{1/3})^2}.$$

$$(5)$$

The dotted and dash-dotted lines in Figs. 15 and 16 indicate values one standard deviation above and below the best-fit value, respectively.

V. DISCUSSION

One discussion should be given on the feedback of the isovector potential U_1 to the potentials used to construct distorted waves in the entrance and exit channels in the DW analysis. These correction terms are $\pm 2 U_1 (N-Z)^{1/2}/A$ for the proton and neutron channels, respectively, and less than a several percent of the distorting potential strengths. Their effects on the final results may be therefore ignored. The data were reanalyzed by using the corrected optical potential parameters. It was indeed found that the contributions from the correction terms were negligibly small, and the results in the

FIG. 16. Same as Fig. 4, but for r_I and a_I.

previous section are hardly changed.

In the present study, the imaginary part of U_1 was taken as free parameters, whereas the strength of this term has so far been thought to be one half of the real part [6,15]. As seen in Fig. 5, the A dependence of the imaginary depth is weaker than that derived from $W_1 = 1/2V_1$. It seems almost constant and about 6 MeV over the mass region studied. When we compare the present results with those of earlier work by Carlson *et al.* at $E_p = 22.8$ MeV [6], although they do not give error estimates and furthermore they have limited the applicable region as $A \geqslant 40$ ($A^{1/3} \geqslant 3.420$), almost the same results were obtained for the geometrical parameters r_I and a_I except that the present values are less $A^{1/3}$ dependent. As a result of the difference in the incident proton energies, the magnitudes of the present V_1 are 20% smaller than those of Ref. [6].

To summarize, analog transitions have been observed at $E_p = 35$ MeV in (p,n) reactions on 13 target nuclei ranging 17$\leqslant A \leqslant$48, ^{17,18}O, ^{22}Ne, ^{25,26}Mg, ^{30}Si, ^{34}S, ^{38,40}Ar, and ^{42,44,48}Ca. Pure $\Delta J^\pi = 0^+$ Fermi-type transitions were observed for six of them. As for the other seven nuclei, contributions from mixed $\Delta J^\pi \neq 0^+$ components or those from unresolved transitions were evaluated by microscopic DWBA calculations to subtract them from the raw data and extract pure Fermi-type transition strengths. The best-fit parameters for the Lane-type isovector potential (V_1, W_1, r_I, a_I) were obtained for each transition, and then each parameter was expressed as a linear function of $A^{1/3}$. The values of V_1 were determined by the present parametrization within $\pm 3 - \pm 5\%$ accuracy in the mass region studied. It was found that W_1 is almost independent of $A^{1/3}$.

[1] A. M. Lane, Phys. Rev. **8**, 171 (1962).

[2] H. Orihara, T. Murakami, S. Nishihara, T. Nakagawa, K. Maeda, K. Miura, and H. Ohnuma, Phys. Lett. **106B**, 171 (1981).

[3] T. Murakami, S. Nishihara, T. Nakagawa, S. Morita, H. Orihara, K. Maeda, and K. Miura, Nucl. Phys. **A377**, 163 (1982).

[4] K. Maeda, H. Orihara, T. Murakami, S. Nishihara, T. Nakagawa, K. Miura, and H. Ohnuma, Nucl. Phys. **A403**, 1 (1983).

[5] T. Suzuki, H. Sagawa, and G. Colò, Phys. Rev. C **54**, 2954 (1996).

[6] J. D. Carlson, C. D. Zafiratos, and D. A. Lind, Nucl. Phys. **A249**, 29 (1975).

[7] K. Furukawa, H. Orihara, M. Kabasawa, T. Kawamura, Y. Takahashi, A. Satoh, T. Niizeki, T. Nakagawa, K. Maeda, K. Ishii, K. Miura, B. A. Brown, and H. Ohnuma, Phys. Rev. C **36**, 1686 (1987); K. Furukawa, Ph.D. thesis, Tohoku University, 1986.

[8] H. Orihara, T. Niizeki, M. Ohura, M. Hosaka, G. C. Jon, K. Ishii, Y. Takahashi, A. Satoh, J. Takamatsu, T. Nakagawa, K. Maeda, K. Miura, and H. Ohnuma, Phys. Rev. C **41**, 2414 (1990).

[9] G. C. Kiang, H. Orihara, Y. Takahashi, A. Satoh, T. Niizeki, J. Takamatsu, M. Kabasawa, T. Kawamura, K. Furukawa, T. Nakagawa, K. Maeda, K. Ishii, K. Miura, L. L. Kiang, P. K. Teng, and H. Ohnuma, Nucl. Phys. **A499**, 339 (1989).

[10] M. Oura, H. Orihara, M. Hosaka, G. C. Jon, A. Terakawa, K. Ishii, A. Narita, K. Hosomi, T. Nakagawa, K. Miura, H. Ohnuma, T. Niizeki, and D. Dehnhard, Nucl. Phys. **A586**, 20 (1995).

[11] B. H. Wildenthal, in *Progress in Particle and Nuclear Physics*, edited by D. H. Wilkinson (Pergamon, London, 1984), Vol. 11, p. 5.

[12] H. Orihara and T. Murakami, Nucl. Instrum. Methods **181**, 15 (1981).

[13] H. Orihara, S. Nishihara, K. Furukawa, M. Kabasawa, T. Kawamura, Y. Takahashi, T. Nakagawa, and K. Maeda, Nucl. Instrum. Methods Phys. Res. A **257**, 189 (1987).

[14] R. Schaeffer and J. Raynal (unpublished).

[15] F. D. Becchetti and G. W. Greenlees, Phys. Rev. **182**, 1190 (1969).

[16] G. Bertsch, J. Borysowics, H. McManus, and W. G. Love, Nucl. Phys. **A284**, 399 (1977).

[17] H. Ohnuma, M. Kabasawa, K. Furukawa, T. Kawamura, Y. Takahashi, A. Satoh, T. Nakagawa, K. Maeda, K. Miura, T. Niizeki, and H. Orihara, Nucl. Phys. **A467**, 61 (1987).

[18] A. E. Echegoyen, W. A. M. Rae, N. S. Goduin, W. A. Richter, C. H. Zimmerman, B. A. Brown, W. E. Ormand, and J. S. Winfield, shell-model code OXBASH, National Superconducting Cyclotron Laboratory Report No. 524 (1984).

[19] W. A. Richter, Nucl. Phys. **A523**, 325 (1991).

[20] A parameter search code for elastic and quasielastic scattering. Quasielastic calculations are made using the Lane model and adopted from the code DWUCK4 originally written by P. D. Kunz.